INTERNATIONAL JOURNAL FOR NUMERICAL METHODS IN FLUIDS, VOL. 22, 921–935 (1996)

APPLICATION OF FLUX-VECTOR-SPLITTING SCHEME TO A DILUTE GAS–PARTICLE JPL NOZZLE FLOW

HSIAO TZU CHANG AND LIH WU HOURNG

Department of Mechanical Engineering, National Central University, Chung Li 32054, Taiwan

AND

LAI CHEN CHIEN

Institute of Physics, Academia Sinica, Taipei 11529, Taiwan

SUMMARY

A time-dependent numerical algorithm is developed for the two-fluid model Euler of TLNS (thin layer Navier–Stokes) equations. The analysis is based on a MUSCL (monotone upstream central scheme for conservation laws)-type flux-vector-splitting scheme with the multi-level technique. This algorithm is applied to investigate JPL (Jet Propulsion Laboratory) nozzle flow. Calculated results for both one- and two-phase flows are given to show the accuracy, the computational efficiency and the particle influence on the flow field.

KEY WORDS: two-phase flow; multilevel

1. INTRODUCTION

For a solid propellant rocket motor design the accurate analysis of flows throughout the entire passage of a nozzle is very important. Experimental studies of JPL nozzle flow have been presented by Cuffel and co-workers[1–3] and many investigations have appeared in the literature.[4–6] Usually the solid propellant exhaust stream contains alumina oxide particles. In these flows, transfer of momentum and heat between gas and particles often dissipates energy in the gas, resulting in a decrease in the nozzle efficiency. Therefore a two-phase flow study is necessary for evaluating the rocket motor's performance.

In 1982 Crowe[7] reviewed the numerical models for dilute gas–particle flows. Generally speaking, there are two approaches commonly used. One is the two-fluid model (or Eulerian–Eulerian) approach and the other is the trajectory (or Eulerian–Lagrangian) approach. The former model treats the two phases as separate media similar to two single phases, where the effect of two-way coupling is incorporated as source terms. Chang[8] used a two-fluid model to solve inviscid JPL nozzle flow by a MacCormack algorithm. The two-fluid model has the advantage of using numerical procedures already established for single-phase flow. In the second approach the gas flow is initially solved without particles. Particle trajectories are then calculated through the gas flow field. Particle source terms are evaluated at each cell. The gas flow is then resolved with these source terms. This process is repeated until the flow field ceases to change. The second method is more easily adaptable to multi-size particles. Hwang and Chang[9] applied the trajectory model and MacCormack scheme to the same JPL nozzle flow problem.

CCC 0271–2091/96/100921–15
© 1996 by John Wiley & Sons, Ltd.

Received November 1993
Revised August 1995

The MacCormack scheme lacks dissipation. In practice an extra artificial dissipation term is needed to overcome numerical oscillation and instability problems. The upwind scheme incorporates the natural dissipation. Thus no additional artificial viscosity is required as in the MacCormack scheme. The purpose of this paper is to apply the flux-vector-splitting algorithm to solve two-phase model flow. A multi-level technique is developed to reduce the computational time. This algorithm is applied to investigate both Euler and TLNS JPL nozzle flow to show performance inefficiences arising from the effect of particles.

2. MATHEMATICAL MODEL

2.1. *Governing equations*

For high-Reynolds-number flow problems the complete Navier–Stokes equations can be approximated by the TLNS equations, where the viscous terms containing derivatives in the direction parallel to the body surface are neglected. Considering the particles as a continuum fluid, the assumptions concerning the particles are as follows. (i) The particles are solid spheres with a uniform diameter. (ii) The volume of each particle is very small and can be neglected; therefore there is no particle pressure. (iii) The gas and particles do not undergo phase changes, so there is no mass coupling. (iv) For dilute particles there are no interactions between the particles. (v) The exchange between the two phases is the Stokes drag force for momentum transfer and convection for heat transfer.

Under the above assumptions the dimensionless axisymmetric governing equations expressed in curvilinear co-ordinates are

$$\frac{\partial Q}{\partial t}+\frac{\partial E}{\partial \xi}+\frac{\partial F}{\partial \eta}=\frac{1}{Re}\frac{\partial F_{\mathrm{v}}}{\partial \eta}+H, \tag{1}$$

$$Q=\frac{1}{J}\begin{bmatrix}\rho\\ \rho u\\ \rho v\\ e\\ (N-1)\rho_{\mathrm{p}}\\ (N-1)\rho_{\mathrm{p}}u_{\mathrm{p}}\\ (N-1)\rho_{\mathrm{p}}v_{\mathrm{p}}\\ (N-1)h_{\mathrm{p}}\end{bmatrix},\qquad E=\frac{1}{J}\begin{bmatrix}\rho U\\ \rho uU+\xi_x P\\ \rho vU+\xi_y P\\ (e+P)U\\ (N-1)\rho_{\mathrm{p}}U_{\mathrm{p}}\\ (N-1)\rho_{\mathrm{p}}u_{\mathrm{p}}U_{\mathrm{p}}\\ (N-1)h_{\mathrm{p}}U_{\mathrm{p}}\end{bmatrix},\qquad F=\frac{1}{J}\begin{bmatrix}\rho V\\ \rho uV+\eta_x P\\ \rho vV+\eta_y P\\ (e+P)V\\ (N-1)\rho_{\mathrm{p}}V_{\mathrm{p}}\\ (N-1)\rho_{\mathrm{p}}u_{\mathrm{p}}V_{\mathrm{p}}\\ (N-1)\rho_{\mathrm{p}}v_{\mathrm{p}}V_{\mathrm{p}}\\ (N-1)h_{\mathrm{p}}V_{\mathrm{p}}\end{bmatrix},$$

$$F_{\mathrm{v}}=\frac{1}{J}\begin{bmatrix}0\\ \alpha_1 u_\eta+\alpha_2 v_\eta\\ \alpha_2 u_\eta+\alpha_3 v_\eta\\ \alpha_4[e/\rho-0{\cdot}5(u^2+v^2)]_\eta+(\alpha_1 u+\alpha_2 v)u_\eta+(\alpha_2 u+\alpha_3 v)v_\eta\\ 0\\ 0\\ 0\\ 0\end{bmatrix},$$

$$H=\frac{1}{J}\left\{\frac{1}{y}\begin{bmatrix}-\rho v\\ -\rho uv\\ -\rho v^2\\ -(e+P)v\\ -(N-1)\rho_\mathrm{p}v_\mathrm{p}\\ -(n-1)\rho_\mathrm{p}u_\mathrm{p}v_\mathrm{p}\\ -(N-1)\rho_\mathrm{p}v_\mathrm{p}^2\\ -(N-1)h_\mathrm{p}v_\mathrm{p}\end{bmatrix}+\frac{1}{J}\begin{bmatrix}0\\ -(N-1)\rho_\mathrm{p}(u-u_\mathrm{p})/t_\mathrm{m}\\ -(N-1)\rho_\mathrm{p}(v-v_\mathrm{p})/t_\mathrm{m}\\ -(N-1)\rho_\mathrm{p}\left(\dfrac{T-T_\mathrm{p}}{t_\mathrm{t}}\dfrac{1}{\gamma-1}+\dfrac{(u-u_\mathrm{p})u_\mathrm{p}+(v-v_\mathrm{p})v_\mathrm{p}}{t_\mathrm{m}}\right)\\ 0\\ (N-1)\rho_\mathrm{p}(u-u_\mathrm{p})/t_\mathrm{m}\\ (N-1)\rho_\mathrm{p}(v-v_\mathrm{p})/t_\mathrm{m}\\ (N-1)\rho_\mathrm{p}\left(\dfrac{T-T_\mathrm{p}}{t_\mathrm{t}}\dfrac{1}{\gamma-1}+\dfrac{(u-u_\mathrm{p})u_\mathrm{p}+(v-v_\mathrm{p})u_\mathrm{p}}{t_\mathrm{m}}\right)\end{bmatrix}\right\},$$

where the subscript 'p' denotes particles. The weak conservation form of the system equations can be reduced to the Euler form (by omitting the viscous flux vector term F_v) or to the TLNS equations. The system can also be used for one-phase (gas only) flow with $N=1$ or for two-phase flow with $N=2$.

Here the contravariant velocities are $U=\xi_x u+\xi_y v$ and $V=\eta_x u+\eta_y v$. The metric terms are $\xi_x=Jy_\eta$, $\xi_y=-Jx_\eta$, $\eta_x=-Jy_\xi$ and $\eta_y=Jx_\xi$, with J^{-1} the cell volume. The total energy of the gas is

$$e=\frac{P}{\gamma-1}+0{\cdot}5\rho(u^2+v^2)$$

and that of the particles is

$$h_\mathrm{p}=\rho_\mathrm{p}\left(T_\mathrm{p}\frac{\bar{C}_\mathrm{s}}{\bar{C}_\mathrm{p}}\frac{1}{\gamma-1}+0{\cdot}5\left(u_\mathrm{p}^2+v_\mathrm{p}^2\right)\right),$$

where $\bar{C}_\mathrm{s}$ is the particle specific heat and $\bar{C}_\mathrm{p}$ is the gas specific heat (the overbar indicates a dimensional quantity). The coefficients in the viscous vector F_v are

$$\alpha_1=(\tfrac{4}{3}\eta_x^2+\eta_y^2)\mu,\qquad \alpha_2=\tfrac{1}{3}\eta_x\eta_y\mu,\qquad \alpha_3=(\eta_x^2+\tfrac{4}{3}\eta_y^2)\mu,$$

$$\alpha_4=\gamma(\eta_x^2+\eta_y^2)\left(\frac{\mu_\mathrm{l}}{Pr_\mathrm{l}}+\frac{\mu_\mathrm{t}}{Pr_\mathrm{t}}\right),\quad \text{with } Pr_\mathrm{l}=0{\cdot}72,\quad Pr_\mathrm{t}=0{\cdot}9,$$

and

$$\mu=\mu_\mathrm{l}+\mu_\mathrm{t},\qquad \mu_\mathrm{l}=T^{3/2}\frac{1+C}{T+C},\qquad \mu_\mathrm{t}\ \text{determined by turbulence model},$$

$$T=\frac{\gamma P}{\rho},\qquad C=\frac{110{\cdot}4}{\bar{T}_\mathrm{ref}},\qquad Re=\frac{\bar{\rho}_\mathrm{ref}\bar{a}_\mathrm{ref}\bar{L}_\mathrm{ref}}{\bar{\mu}_\mathrm{ref}}.$$

The momentum relaxation time is given as

$$t_\mathrm{m}=\frac{t_{\mathrm{m}0}}{A_0},\tag{2}$$

where $t_{\mathrm{m}0}=\frac{1}{18}(\bar{\rho}_\mathrm{s}\bar{d}_\mathrm{p}^2/\bar{\mu}_\mathrm{l})\,\bar{a}_\mathrm{ref}/\bar{L}_\mathrm{ref}$ and $A_0=C_\mathrm{D}/C_{\mathrm{D\ Stokes}}$, with $\bar{\rho}_\mathrm{s}$ the particle intrinsic density and $\bar{d}_\mathrm{p}$ the particle diameter. The relationship between ρ_p and ρ_s is $\rho_\mathrm{p}=N_\mathrm{p}(\pi/6)\rho_\mathrm{s}d_p^3/\mathscr{V}$, where N_p is the number of particles in the control volume $\mathscr{V}$. The particle drag coefficient C_D depends on the relative Mach number

$$Mn_\mathrm{p}=\frac{\surd[(u-u_\mathrm{p})^2+(v-v_\mathrm{p})^2]}{a},\qquad a=\sqrt{\left(\frac{\gamma P}{\rho}\right)},$$

and the relative Reynolds number

$$Re_{\mathrm{p}} = \frac{\bar{\rho}\bar{d}_{\mathrm{p}}\bar{a}_{\mathrm{ref}}}{\bar{\mu}_{\mathrm{l}}}\sqrt{[(u-u_{\mathrm{p}})^2+(v-v_{\mathrm{p}})^2]}, \qquad \bar{\rho} = \rho\bar{\rho}_{\mathrm{ref}}, \qquad \bar{\mu} = \mu\bar{\mu}_{\mathrm{ref}}.$$

In the present study, since Mn_{p} is small ($Mn_{\mathrm{p}} < 0{\cdot}5$), the effect of Mn_{p} on C_{D} can be neglected. The empirical drag coefficients are[10]

$$C_{\mathrm{D}} = \frac{24}{Re_{\mathrm{p}}}\left(1+0{\cdot}15Re_{\mathrm{p}}^{0{\cdot}687}\right)+\frac{0{\cdot}42}{1+4{\cdot}25\times 10^4 Re_{\mathrm{p}}^{-1{\cdot}16}} \quad \text{for } Re_{\mathrm{p}} < 3\times 10^5, \qquad C_{\mathrm{D\,Stokes}} = \frac{24}{Re_{\mathrm{p}}}.$$

The energy relaxation time is given as

$$t_{\mathrm{t}} = \frac{t_{\mathrm{t0}}}{B_0}, \tag{3}$$

where $t_{\mathrm{t0}} = \frac{3}{2}t_{\mathrm{m0}}Pr_{\mathrm{l}}$ and $B_0 = Nu/Nu_{\mathrm{Stokes}}$. The empirical Nusselt numbers are[11]

$$Nu = 2+0{\cdot}459Re_{\mathrm{p}}^{0{\cdot}55}Pr_{\mathrm{l}}^{0{\cdot}33}, \qquad Nu_{\mathrm{Stokes}} = 2.$$

2.2. *Turbulence model*

An algebraic two-layer Baldwin–Lomax turbulence model[12] is used in this study. The Baldwin–Lomax model is efficient and accurate compared with more complex models. The interaction of the gas flow and the solid particle turbulence is complex and not well understood at present. In this study Melville and Bray's algebraic eddy viscosity formulation[13] is adopted to describe the influence of the particles on turbulence. The turbulent viscosity coefficient μ_{t} is decreased by the particles in the ratio of the particle loading ρ_{p}/ρ from the corresponding one-phase flow μ_{t0}:

$$\mu_{\mathrm{t}} = \mu_{\mathrm{t0}}\left(1+\frac{\rho_{\mathrm{p}}}{\rho}\right)^{-1}. \tag{4}$$

3. NUMERICAL METHOD

The finite volume approach is used for the formulation of difference equations, i.e. numerical fluxes are defined at the cell interfaces and dependent variables are defined at the centroids. The governing equation (1) can be discretized by an explicit scheme based on the upwind difference of the split flux for the convective terms and the central difference for the viscous term as

$$\begin{aligned} Q_{j,k}^{n+1} - Q_{j,k}^{n} = \Delta Q_{j,k}^{n} &= -\Delta t\left[\left(\frac{\nabla E^{+}}{\Delta\xi}+\frac{\Delta E^{-}}{\Delta\xi}+\frac{\nabla F^{+}}{\Delta\eta}+\frac{\Delta F^{-}}{\Delta\eta}\right)_{j,k}^{n} - \frac{1}{Re}\left(F_{\mathrm{v}j,k+1/2}^{n} - F_{\mathrm{v}j,k-1/2}\right) - H_{j,k}^{n}\right] \\ &= \mathrm{RHS}. \end{aligned} \tag{5}$$

The forward and backward upwind difference operators for the convective term in the ξ-direction are defined by

$$\begin{aligned} \frac{\nabla E^{+n}}{\Delta\xi_{j,k}}+\frac{\Delta E^{-n}}{\Delta\xi_{j,k}} &= \frac{1}{\Delta\xi}[(E_{j,k}^{+n}-E_{j-1,k}^{+n})+(E_{j+1,k}^{-n}-E_{j,k}^{-n})] \\ &= \frac{1}{\Delta\xi}[(E_{j+1,k}^{-n}+E_{j,k}^{+n})-(E_{j,k}^{-n}+E_{j-1,k}^{+n})] \\ &= \frac{1}{\Delta\xi}\{[E^{-}(Q_{j+1/2,k}^{+n})+E^{+}(Q_{j+1/2,k}^{-n})]-[E^{-}(Q_{j-1/2,k}^{+n})+E^{+}(Q_{j-1/2,k}^{-n})]\} \\ &= \frac{1}{\Delta\xi}(E_{j+1/2,k}^{n}-E_{j-1/2,k}^{n}), \end{aligned} \tag{6}$$

where $E^{\pm}$ are the split fluxes and $Q^{-}_{j+1/2,k}$ and $Q^{+}_{j+1/2,k}$ are the upwind-biased and downwind-biased interpolation values at the interface $j + 1/2$ respectively.

3.1. *Flux splitting*

Van Leer flux vector splitting has continuously differentiable flux contributions and has been shown to result in smoother solutions near sonic points.[14] For supersonic flow, $|M_\xi| > 1$,

$$\begin{aligned} E^{+} &= E \quad \text{and} \quad E^{-} = 0, \quad M_\xi > 1, \\ E^{+} &= 0 \quad \text{and} \quad E^{-} = E, \quad M_\xi < -1, \end{aligned} \tag{7}$$

and for subsonic flow, $|M_\xi| < 1$,

$$E^{\pm} = \frac{\text{grad}(\xi)}{J} f_{\text{m}}^{\pm} \begin{bmatrix} 1 \\ \dfrac{\xi_x}{\text{grad}(\xi)}\left(-\dfrac{U}{\text{grad}(\xi)} \pm 2a\right)/\gamma + u \\ \dfrac{\xi_y}{\text{grad}(\xi)}\left(-\dfrac{U}{\text{grad}(\xi)} \pm 2a\right)/\gamma + v \\ h + 0{\cdot}5(u^2 + v^2) \end{bmatrix}, \tag{8}$$

where

$$\text{grad}(\xi) = \surd(\xi_x^2 + \xi_y^2), \qquad M_\xi = \frac{U/\text{grad}(\xi)}{a}, \qquad f_{\text{m}}^{\pm} = \pm\rho a (M_\xi \pm 1)^2/4.$$

Note that the split energy flux was reformulated in contrast with the original version and that the new formulation has the advantage of simplicity and efficiency.[15] For the particle phase flow there is only one eigenvalue in the convective flux, which is split by the Steger and Warming method[16] as

$$E_{\text{p}}^{\pm} = \lambda_{\text{p}}^{\pm} \frac{1}{J} \begin{bmatrix} \rho_{\text{p}} \\ \rho_{\text{p}} u_{\text{p}} \\ \rho_{\text{p}} v_{\text{p}} \\ h_{\text{p}} \end{bmatrix} \qquad \lambda_{\text{p}}^{\pm} = \frac{\lambda_{\text{p}} \pm |\lambda_{\text{p}}|}{2}, \qquad \lambda_{\text{p}} = \xi_x u_{\text{p}} + \xi_y v_{\text{p}}. \tag{9}$$

Here the interface variables are obtained by MUSCL extrapolation with a third-order smooth limiter[14] from cell centre values of the primitive variables $\rho, u, v, p, \rho_{\text{p}}, u_{\text{p}}, v_{\text{p}}$ and T_{p}. It was found that using primivite variables yields better convergence for flows with strong shocks.[17]

3.2. *Time integration*

A two-stage Runge–Kutta method with optimal coefficients[18] of the form

$$Q^{*} = Q^{n} + 0{\cdot}6807\ \text{RHS}(Q^{n}), \tag{10}$$

$$Q^{n+1} = Q^{n} + \text{RHS}(Q^{*}) \tag{11}$$

is used to integrate equation (5) in time, to improve the accuracy and extend the explicit scheme's stability region. Here the gas phase residual RHS is replaced by a weighted average of neighbouring residuals with the implicit residual smoother to increase the available time step used in the Runge–Kutta method:

$$(1 - 0{\cdot}2\delta_\eta^2)(1 - 0{\cdot}2\delta_\xi^2)\text{RHS}^{\text{ave}} = \text{RHS}, \tag{12}$$

where δ_ξ^2 and δ_η^2 are second-difference operators.

For accelerating the convergence to a steady state, a space-varying Δt close to the local stability limit[19,20]

$$\Delta t = \frac{CFL}{|U| + |V| + a\sqrt{(\xi_x^2 + \xi_y^2 + \eta_x^2 + \eta_y^2)}} \tag{13}$$

is used, where *CFL* is taken as 1·0 for Euler flow and 0·6 for turbulence flow.

3.3. *Multi-level technique*

One would like to use a coarse grid system to reduce the computational time in the numerical computations. However, the solution obtained from a coarser mesh is not sufficiently accurate owing to large truncation errors. One way to improve this is the multi-level technique. In the present work the coarse grid is formed by eliminating every second line of the next fine mesh in a crosswise direction. The computation starts from the first coarse mesh, then the flow field properties are interpolated back to the next fine mesh after the structure of the flow field has been built; the particle equations are counted from the second mesh and the viscous diffusion terms are evaluated only on the finest grid. Therefore the computational efficiency is improved while maintaining low truncation errors.

4. INITIAL AND BOUNDARY CONDITIONS

The quiescent gas and particle-free assumptions in the whole field are taken as initial condition and reference data (i.e. $\bar{\rho}_{\mathrm{ref}}, \bar{a}_{\mathrm{ref}}, \bar{P}_{\mathrm{ref}}, \bar{T}_{\mathrm{ref}}, \bar{\mu}_{\mathrm{ref}}$).

At the inlet boundary the chamber total temperature T_{total}, total pressure P_{total} and flow angle are specified. The upstream-running Riemann invariant R^- is extrapolated from the inside domain ('in') to the boundary ('b') as

$$R_{\mathrm{b}}^- = \left(V_{\mathrm{total}} - \frac{2a}{\gamma - 1}\right)_{\mathrm{in}}, \qquad V_{\mathrm{total}} = \sqrt{(u^2 + v^2)}. \tag{14}$$

The total velocity at the inlet, $V_{\mathrm{total_b}}$, is found from the total temperature and isentropic relations[20]

$$V_{\mathrm{total_b}} = \frac{(\gamma - 1)R_{\mathrm{b}}^- + \sqrt{[2(1-\gamma)(R_{\mathrm{b}}^-)^2 + 4(\gamma + 1)C_{\mathrm{p}}T_{\mathrm{total}}]}}{\gamma + 1}, \tag{15}$$

$$a_{\mathrm{b}} = \frac{\gamma - 1}{2}(V_{\mathrm{total_b}} - R_{\mathrm{b}}^-). \tag{16}$$

The quantities ρ and P are then determined by isentropic relations. For two-phase flow the particle mass fraction $\phi = \rho_{\mathrm{p}}/(\rho + \rho_{\mathrm{p}})$, velocity lag and temperature ratio are also specified at the inlet.

For subsonic outflow the exit static pressure is specified and the other variables are extrapolated from those in the interior. For supersonic outflow all flow variables are extrapolated from upstream.

On the axisymmetric line the symmetric boundary conditions require that the normal gradients of density, tangential velocity, gas pressure and particle temperature be zero. The normal velocity is also set to zero.

On the solid surface the velocity must meet the tangent condition for Euler flow and the no-slip condition for viscous flow. All other flow variables are found by extrapolation, except for ρ and p for Euler flow which are determined by the Riemann invariant and entropy equations

$$a_{\mathrm{b}} = \frac{\gamma - 1}{2}\left(\frac{2a_{\mathrm{in}}}{\gamma - 1} + V_{\mathrm{n_{in}}}\right), \qquad V_{\mathrm{n}} = \frac{\eta_x + \eta_y v}{\sqrt{(\eta_x^2 + \eta_y^2)}}, \tag{17}$$

$$\rho_{\mathrm{b}} = \left(\frac{1}{\gamma} a_{\mathrm{b}}^2 \frac{\rho_{\mathrm{in}}^{\gamma}}{P_{\mathrm{in}}}\right)^{1/(\gamma-1)}, \qquad P_{\mathrm{b}} = \frac{\rho_{\mathrm{b}}}{\gamma} a_{\mathrm{b}}^2. \tag{18}$$

5. RESULTS

5.1. *Grid system*

Consider the JPL axisymmetrical 45°–15° convergent–divergent conical nozzle. Figure 1 shows the 190×41 and 190×51 grid systems for Euler and viscous flows respectively. The length scales are non-dimensionalized by the throat diameter $\bar{L}_{\mathrm{ref}} = 0{\cdot}0406$ m. The grid systems are generated by the solution of the Poisson equation, which automatically generates a smoothly varying grid that conforms to an arbitrary body and allows grid point clustering near the boundary.[21]

5.2. *One-phase flow*

The fluid is initially set at sea level with zero velocity. Under reservoir conditions of $\bar{T}_{\mathrm{total}} = 555\,k$, $\bar{P}_{\mathrm{total}} = 10{\cdot}34 \times 10^5$ N/m^2 and zero inflow velocity angle the flow is accelerated from subsonic to supersonic in the nozzle. Figure 2 depicts the variation in Mach number along the wall and centreline in the Euler computation. For comparison, experimental data[1–3] and previous numerical results[4,6] are also plotted in Figure 2. It is seen that the present predictions agree well with the

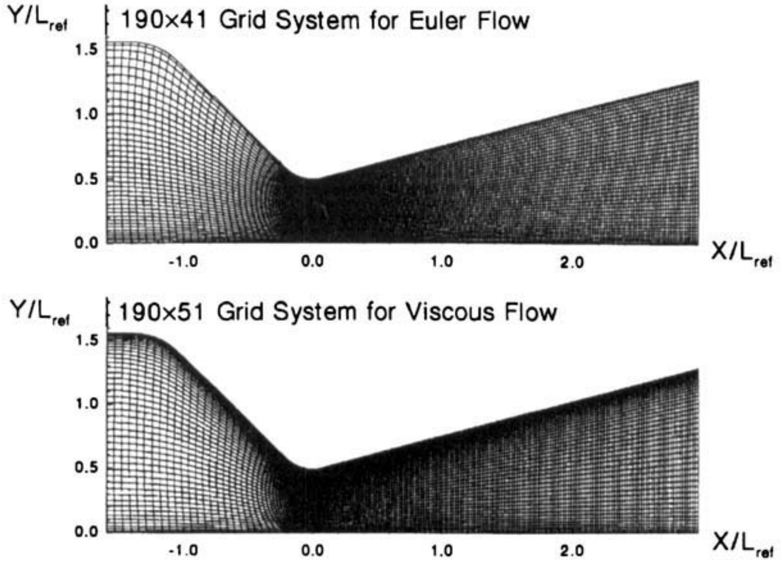

Figure 1. Grid system

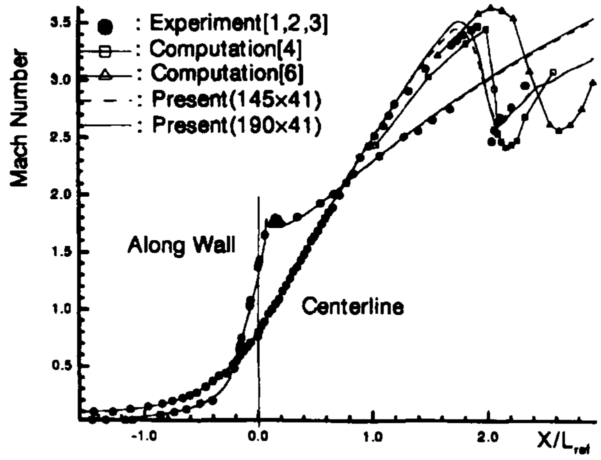

Figure 2. Mach number profiles for Euler one-phase flow

experimental data. The difference between the coarser (145 × 41) and finer (190 × 41) grid solutions is slight, so we can conclude that the solution will only be minimally affected by further grid refinement. Serra[4] gives a sharper shock profile, but it is undershot after the shock. Liang and Chan's[6] results fail to predict the shock location. Since the nozzle contour has a rapid contraction followed by a throat with a small radius of curvature, the flow near the throat wall is overturned and inclinded to the downstream wall. A weak shock is thus formed to turn the flow parallel to the wall. From the inlet the Mach number increases more rapidly along the wall than along the centreline. In the throat plane the Mach number is 1·3 on the wall and 0·8 on the axis. Along the wall the Mach number decreases slightly from 1·79 to 1·72 near the circular throat and divergent junction and then increases slowly in the downstream direction. Along the centerline the Mach number increases linearly until $X/L_{\mathrm{ref}} = 1{\cdot}97$ and then drops suddenly from 3·5 to 2·6. The reductions in Mach number near the throat wall and downstream centreline are related to the shock wave. In Figure 3 the calculated Mach number contours exhibit a weak oblique shock emanating from the throat wall and intersecting the downstream centreline and then being reflected.

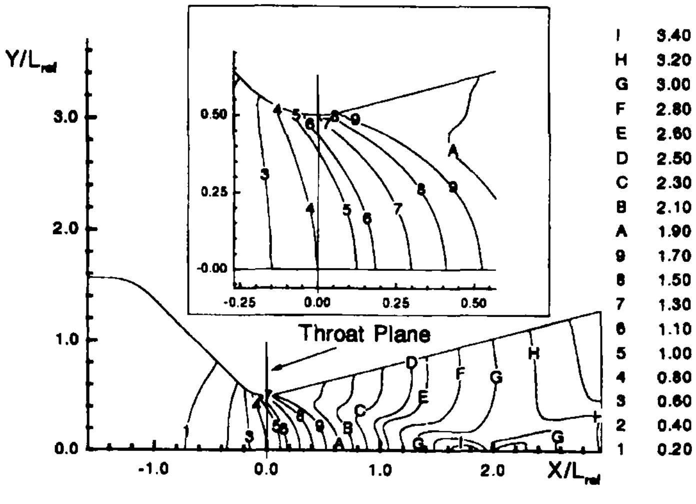

Figure 3. Mach number contours for Euler one-phase flow

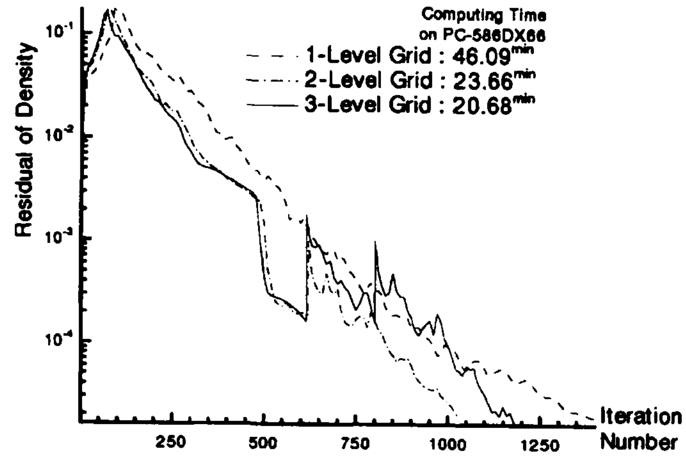

Figure 4. Convergence histories for Euler one-phase flow

The convergence histories are shown in Figure 4 using one-, two- and three-level mesh procedures respectively. There exist large discontinuities which reflect the perturbation of the numerical solution due to multi-level grid changes. The three-level case is the best. The computing time is much reduced from 46·09 min for the single-mesh case to 20·68 min for the three-level mesh case on a PC-586DX66 computer. By employing the present multi-level strategy, only 45% of the computational time with a conventional fixed grid is needed. In this aspect the present numerical procedure can be regarded as an efficient one.

Calculations are also carried out to study the effect of viscosity on the flow structure. The JPL nozzle viscous flow is considered for $Re = 9{\cdot}46 \times 10^5$ (based on the throat diameter at sea level). The turbulence boundary layer alters the apparent size of the nozzle and thus shifts the supersonic Mach contours backwards and changes the shock wave position forwards, as shown by the Mach number profiles and contours in Figure 5.

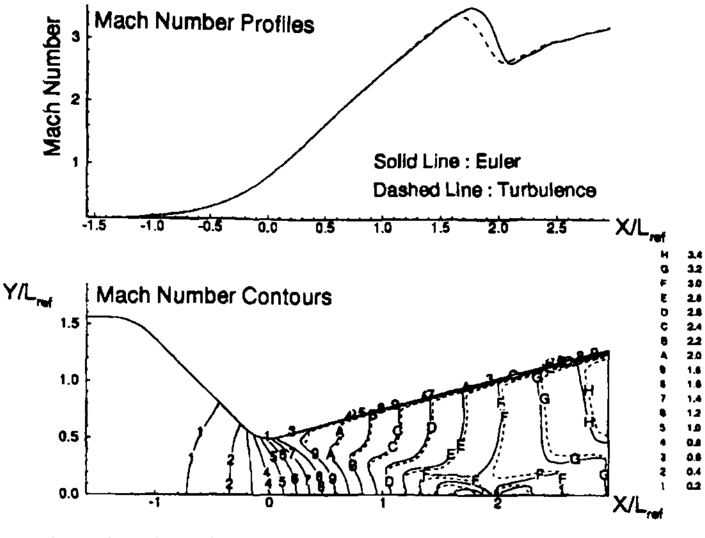

Figure 5. Comparison of Mach number profiles and contours between Euler and turbulent one-phase flows

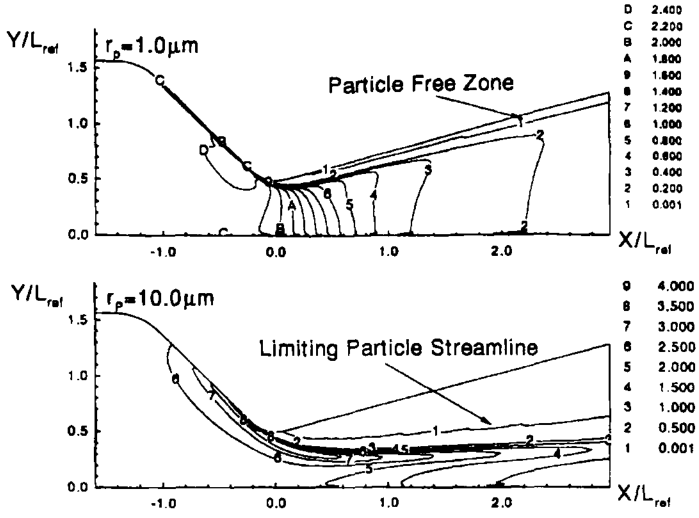

Figure 6. Particle density contours $\rho_p/_{\text{ref}}$ for Euler flow

5.3. *Two-phase flow*

For the gas-particle fully coupled flow simulation, related data presented by Chang[8] are used:

$$\bar{C}_s = 1{\cdot}38 \times 10^3\ \text{J kg}^{-1}\ \text{K}^{-1}, \quad \bar{C}_p = 1{\cdot}07 \times 10^3\ \text{J kg}^{-1}\ \text{K}^{-1}, \quad \bar{\rho}_s = 4004{\cdot}62\ \text{kg m}^{-3}.$$

Two different-sized particles with the same mass fraction $\phi = 0{\cdot}3$ are considered. The particle radii $\bar{r}_p$ are 1·0 and 10·0 μm. The inlet velocity and temperature of the particles are presumed to be the same as those of the gas phase.

5.3.1. Particle trajectories. For most flows the domain occupied by the particles is less than the entire flow region. There is a limiting particle streamline marking the particle-free zone (defined as $\rho_p/\rho_{\text{ref}} < 0{\cdot}001$). Several ranges of particle concentration occur in the particle domain.

Figure 6 shows the Euler flow particle density contours for the two different sizes of particles. Although the gas is simplified as inviscid, the Stokes drag force is not assumed to be negligible. For the small particles the drag force is greater than the inertia force, so particles can more easily be carried by the gas flow. On the other hand the large particles cannot effectively turn around the throat corner because their inertia tends to retain their initial momentum. The particle-free zone downstream of the throat is much greater for the large particles than for the small particles. Restricted by the nozzle contour, there exists a particle concentration range near the convergent wall and the partial density contours are clustered under the limiting particle streamline, especially in the case of the large particles.

The convergence histories of the small-particle flow simulation are presented in Figure 7 to show the multi-level efficiency. Even though the total numbers of iterations are almost the same for the single-level and three-level simulations, the computing time is shortened from 127·16 min to 75·02 min, i.e. only 59 per cent of the computational time is needed for the latter.

Computational results of particle density contours by TLNS are shown in Figure 8. The viscous effect reduces the inertia force in the boundary layer. There is an obvious particle-free zone starting from near the inlet along the wall. Therefore the particle-free zone for the small particles is larger in the downstream region than that in the corresponding Euler case. The large particles with large inertia tend

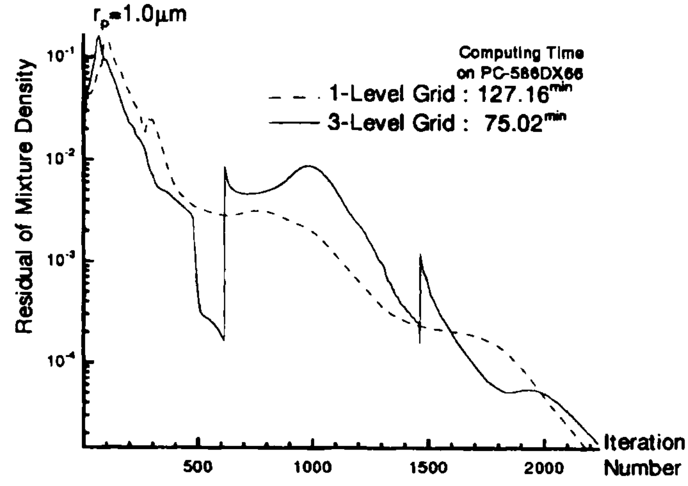

Figure 7. Convergence histories for Euler two-phase flow

to keep their initial momentum and impact on the convergent surface again. This situation can be clearly seen from the velocity vector analysis in Figures 9 and 10.

5.3.2. Effect on flow properties. Since the particle density is larger than the gas density, in two-phase flow the gas velocity is reduced by the particles. The influence of particles on the fluid flow depends on size and number of particles. The smaller the particle size, the smaller is the relaxation time required. The interaction between the two-phase flow is thus increased. For a fixed mass fraction a decrease in the particle size means that more particles are present in the flow and the interaction is also strengthened. Figure 11 shows the gas Mach number distributions along the wall and centreline for Euler one- and two-phase flows. The gas Mach number is reduced in the two-phase flow field and the

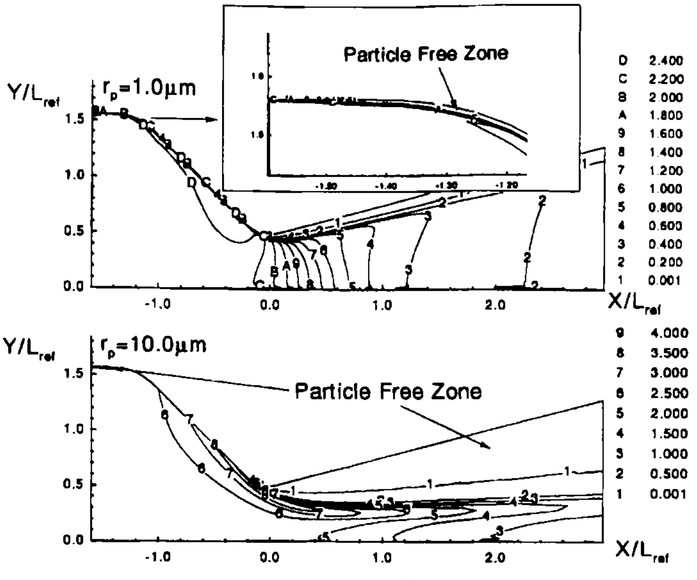

Figure 8. Particle density contours ρ_p/ρ_{ref} for turbulent flow

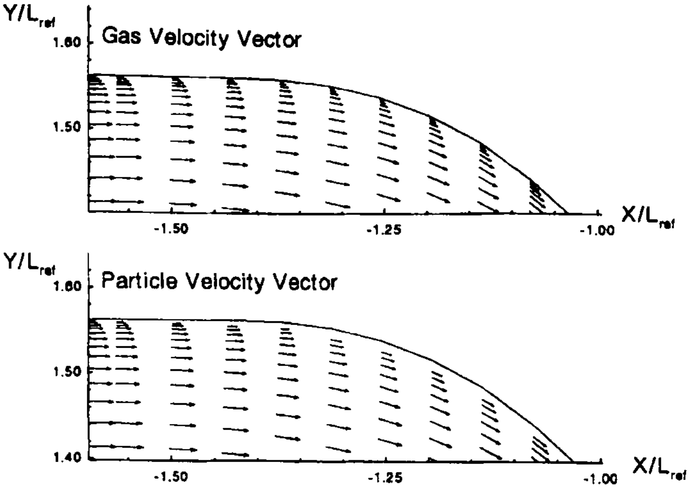

Figure 9. Small-particle velocity vectors for turbulent flow

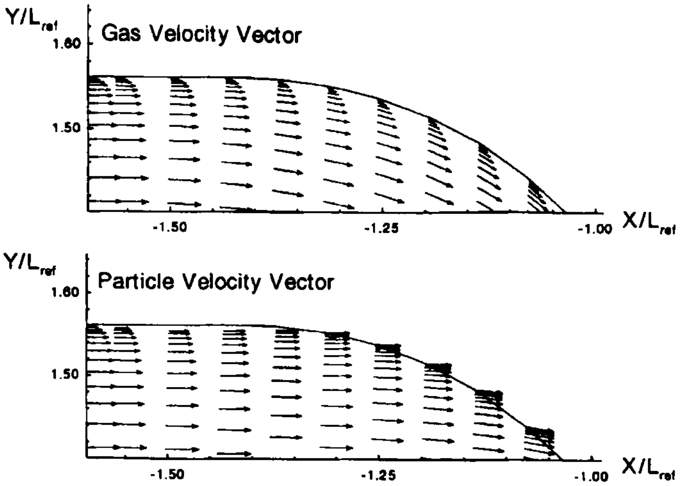

Figure 10. Large-particle velocity vectors for turbulent flow

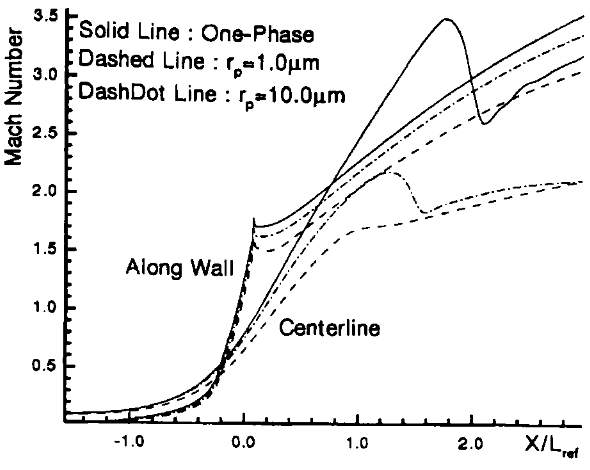

Figure 11. Mach number profiles for Euler one- and two-phase flows

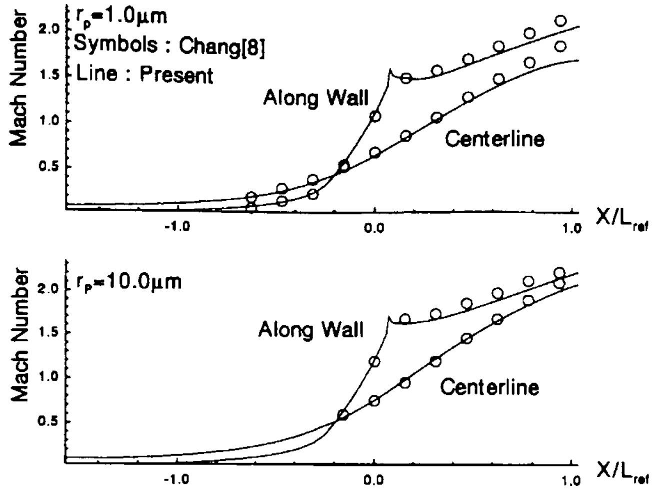

Figure 12. Comparison of Euler two-phase Mach number distributions with previous work

reduction becomes large for the case with the small particles. Owing to the particle-free zone, the Mach number difference between the one- and two-phase flows along the wall is smaller than that at the centreline. This is physically correct. A comparison of the present results with previous numerical calculations[8] is shown in Figure 12. The agreement among all the computations is generally good. Similar phenomena also occur for the viscous flow. However, large changes in the Mach number contours as compared with the one-phase flow can be found in Figure 13. For the two-phase flow there is a greater velocity gradient along the limiting particle streamline due to the high gradient of the particle concentration.

The temperature distributions along the centreline are plotted in Figure 14. This indicates that the gaseous flow for the two-phase flow is heated by the hot particles. A comparison of Euler and TLNS gas temperature profiles along the wall is plotted in Figure 15. Because of the high concentration of hot

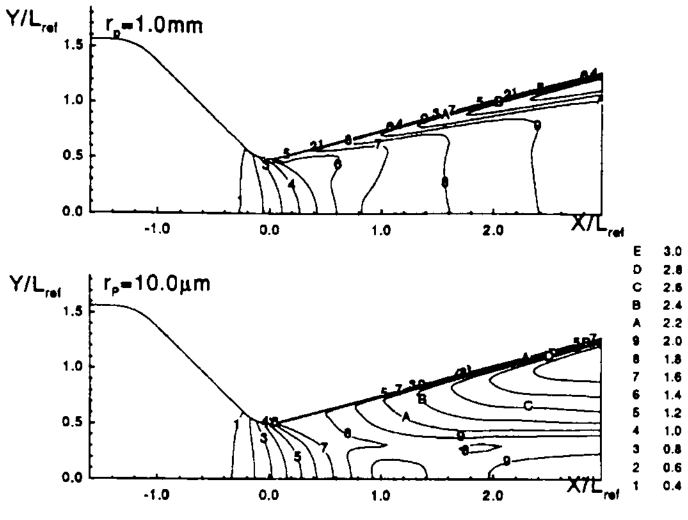

Figure 13. Mach number contours for turbulent two-phase flow

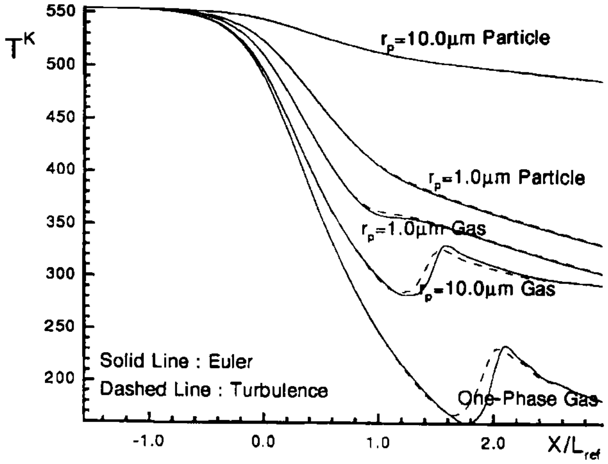

Figure 14. Comparisonm of Euler and turbulent flow temperature profiles along centreline

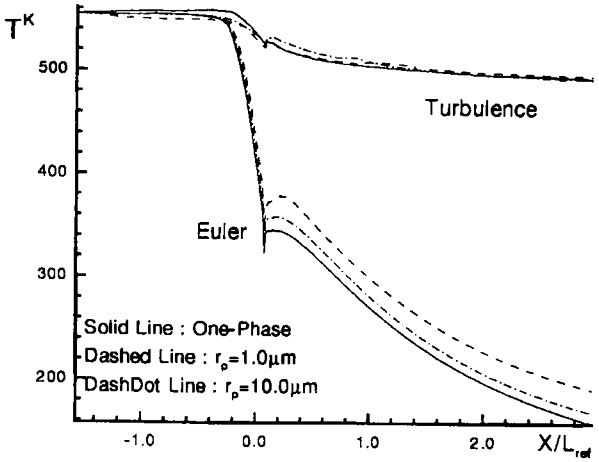

Figure 15. Comparison of Euler and turbulent flow gas temperature profiles along wall

particles on the centreline, the temperature difference between one-and two-phase gas at the wall is smaller than that at the centreline.

The thrust of the JPL nozzle estimated by isentropic theory[22] is 2165 N. The results of numerical calculation by

$$F = \dot{m}V_e + A_eP_e = (\rho_e V_e + P_e)A_e \tag{19}$$

are given in Table I.

Table I. JPL nozzle thrust

	One-phase	$r_p = 1{\cdot}0\ \mu m$	$r_p = 10{\cdot}0\ \mu m$
Euler	2114 N	1636 N	1948 N
Turbulent	2082 N	1595 N	1900 N

As seen in the table, the Euler one-phase flow result is close to that of classical theory. In turbulent flow the viscous effect dissipates approximately 2 per cent thrust compared with Euler flow. A significant loss in thrust is due to the low velocity of the gas flow and heat unconverted to directed kinetic energy in two-phase flow. For small particles the gas–particle interaction is more violent and the thrust loss is increased to 23 per cent. The thrust loss due to large particles is about 8 per cent. Therefore the two-phase effect is more serious than the viscous effect and cannot be neglected.

6. CONCLUSIONS

Since the MUSCL-type flux-vector-splitting scheme possesses natural dissipation, no additional artificial viscosity is required as it is for the MacCormack scheme to stabilize the computation. The numerical computation proves that the multi-level technique is an effective tool for solving both one- and two-phase flows. Results show good accuracy when compared with experimental data for Euler one-phase flow. The method is extended to solve TLNS and two-phase flow; the computational results are physically reasonable and also in good agreement with previous studies. The presence of particles has a dramatic effect on the nozzle flow field and thrust. To investigate a real two-phase flow, it is not permissible to use the single-phase model.

REFERENCES

1. L. H. Back and R. F. Cuffel, 'Detection of oblique shocks in a conical nozzle with a circular-arc throat', *AIAA J.*, **4**, 2219–2221 (1966).
2. L. H. Back, P. F. Massier and R. F. Cuffel, 'Flow phenomena and convective heat transfer in a conical supersonic nozzle', *J. Spacecraft*, **4**, 1040–1047 (1967).
3. R. F. Cuffel, L. H. Back and P. F. Massier, 'Transonic flowfield in a supersonic nozzle with small throat radius of curvature', *AIAA J.*, **7**, 1364–1366 (1969).
4. R. A. Serra, 'Determination of internal gas flows by a transient numerical technique', *AIAA J.*, **10**, 603–611 (1972).
5. C. K. Lombard, J. Bardina, E. Venkatapathy and J. Oliger, 'Multidimensional formulation of CSCM—an upwind flux difference eigenvector split method for the compressible Navier–Stokes equations', *AIAA Paper 83–1895*, 1983.
6. P. Liang and D. C. Chan, 'Development of a robust pressure-based numerical scheme for spray combustion applications', *AIAA Paper 93–0902*, 1993.
7. C. T. Crowe, 'Review—numerical models for dilute gas–particle flows', *J. Fluids Eng.*, **104**, 297–303 (1982).
8. I. S. Chang, 'One- and two-phase nozzle flows', *AIAA J.*, **18**, 1455–1461 (1980).
9. C. J. Hwang and G. C. Chang, 'Numerical study of gas–particle flow in a solid rocket nozzle', *AIAA J.*, **26**, 682–689 (1988).
10. R. Clift, J. R. Grace and M. E. Weber, *Bubbles, Drops, and Particles*, Academic Press, New York, 1978.
11. D. J. Carlson and R. F. Hoglund, 'Particle drag and heat transfer in rocket nozzles', *AIAA J.*, **2**, 1980–1984 (1964).
12. B. S. Baldwin and H. Lomax, 'Thin layer approximation and algebraic model for separated turbulent flows', *AIAA Paper 78–257*, 1978.
13. W. K. Melville and K. N. C. Bray, 'A model of the two-phase turbulent jet', *Int. J. Heat Mass Transfer*, **22**, 647–656 (1979).
14. W. K. Anderson, J. L. Thomas and B. Van Leer, 'Comparison of finite volume flux vector splittings for the Euler equations', *AIAA J.*, **24**, 1453–1460 (1986).
15. M. S. Liou, B. Van Leer and J. S. Shuen, 'Splitting of inviscid fluxes for real gases', *J. Comput. Phys.*, **87**, 1–24 (1990).
16. J. L. Steger and R. F. Warming, 'Flux vector splitting of the inviscid gasdynamic equations with application to finite-difference methods', *J. Comput. Phys.*, **40**, 263–293 (1981).
17. J. S. Shuen, 'Upwind differencing and LU factorization for chemical non-equilibrium Navier–Stokes equations', *J. Comput. Phys.*, **99**, 233–250 (1992).
18. J. F. Lynn and B. Van Leer, 'Multi-stage schemes for the Euler and Navier–Stokes equations with optimal smoothing', *AIAA Paper 93-3355*, 1993.
19. T. H. Pulliam and J. L. Steger, 'Recent improvements in efficiency accuracy, and convergence for implicit approximate factorization algorithms', *AIAA Paper 85-0360*, 1985.
20. R. V. Chima and J. W. Yokota, 'Numerical analysis of three-dimensional viscous internal flows', *AIAA J.*, **28**, 798–806 (1990).
21. R. L. Sorenson, 'A computer program to generate two-dimensional grids about airfoils and other shapes by the use of Poisson's equation', *NASA TM-81198*, 1980.
22. A. H. Shapiro, *The Dynamics and Thermodynamics of Compressible Fluid Flow*, Vol. 1, Ronald, New York, 1953.